Nanoscale

The Radiation Chemistry of Focused Electron-Beam Induced Etching of Copper in Liquids.

Journal:	*Nanoscale*
Manuscript ID	NR-ART-03-2019-001857.R1
Article Type:	Paper
Date Submitted by the Author:	09-May-2019
Complete List of Authors:	Lami, Sarah; University of Kentucky, Electrical and Computer Engineering Smith, Gabriel ; University of Kentucky, Electrical and Computer Engineering Cao, Eric ; University of Kentucky, Electrical and Computer Engineering Hastings, J. Todd; University of Kentucky, Electrical and Computer Engineering

Journal Name

ARTICLE TYPE

Cite this: DOI: 10.1039/xxxxxxxxxx

The Radiation Chemistry of Focused Electron-Beam Induced Etching of Copper in Liquids†

Sarah K. Lami,[a b] Gabriel Smith,[a] Eric Cao,[a] and J. Todd Hastings[a*]

Received Date
Accepted Date

DOI: 10.1039/xxxxxxxxxx

www.rsc.org/journalname

Well-controlled, focused electron-beam induced etching of copper thin films has been successfully conducted on bulk substrates in an environmental scanning electron microscope by controlling liquid-film thickness with an *in-situ* correlative interferometry system. Knowledge of the liquid-film thickness enables a hybrid Monte Carlo/continuum model of the radiation chemistry to accurately predict the copper etch rate using only electron scattering cross-sections, radical yields, and reaction rates from previous studies. Etch rates depended strongly on the thickness of the liquid film and simulations confirmed that this was a result of increased oxidizing radical generation. Etch rates also depended strongly, but non-linearly, on electron beam current, and simulations showed that this effect arises through the dose-rate dependence of reactions of radical species.

1 Introduction

Electron-beam induced etching of nanostructures in liquids is being intensely investigated to understand both the mechanisms of nanoparticle growth and dissolution [1–7] as well as the chemistry of the liquid environment during *in-situ* electron microscopy. [8–10]. These studies are typically conducted in sealed liquid cells in transmission electron microscopes. In contrast, electron-beam induced etching of functional materials on bulk substrates, or of fabricated nanostructures such as integrated circuits, can be conducted in an environmental scanning electron microscope with the liquid exposed to the low-vacuum environment. This latter approach offers an intriguing alternative to focused electron- and ion-beam induced etching in reactive gases, particularly when no volatile product is produced or when selectivity to other materials is required. [11]

Gas-assisted focused electron and ion beam induced processes are the methods of choice for nanoscale fabrication that requires site-specific deposition or etching of functional materials. [12–14] Common applications include nanoscale rapid prototyping, electrical connection to chemically synthesized structures, semiconductor mask repair, and integrated circuit editing and debugging. [15–17]. In concept, focused electron beam induced processing (FEBIP) and focused ion beam induced processing (FIBIP) are similar. A gaseous reactant is delivered to the substrate; then subsequent ion or electron beam driven reactions lead to gas dissociation that initiates the etching or deposition process. Though faster, the ion-based process can cause sample damage due to ion bombardment and implantation. [15,18–20] Ion implementations can also significantly alter the electrical, mechanical, and optical properties of the sample. In contrast, an electron-based process causes negligible damage to the sample. This advantage has garnered the process considerable attention from researchers, and several different metals have been deposited including gold, [21–23] palladium, [24–27] tungsten, [28] copper, [29,30] silver, [31] and platinum [26–28,32].

As structures continue to scale down across the semiconductor industry following Moore's Law, [33,34] selective material removal has become challenging. Integrated circuits have a wide variety of materials densely packed across a small geometry such as aluminum, copper, silicon dioxide, [35,36] tungsten [37] and dielectric layers of carbon doped oxide. [36,38] As a result, significant efforts have been directed to utilize FEBIE, FIB, and gas-assisted focused ion beam (GA-FIB) as tools for selective etching of technologically important materials. All of these have become vital tools, especially in circuit edit [20,39] and failure analysis. Although these approaches enjoy the benefit of significant previous research and development, they are still limited by several factors. For FIB, these include copper grain orientation dependent, bubble formation, redeposition, ion implantation, and most significantly sample damage. [15,20] For FEBIE the primary challenge is in the limited selection of gaseous reactants that produce volatile by-products along with other precursor limitations such as toxicity and stability. [39,40]

Exposing a liquid reactant, instead of a gas, to the elec-

[a] *Department of Electrical and Computer Engineering, University of Kentucky, Lexington, Kentucky 40506, USA. Fax: +1 (859) 257-3092; Tel: +1 (859) 218-6544; E-mail: todd.hastings@uky.edu*
[b] *AL-Furat AL-Awsat Technical University, Iraq*

† Electronic Supplementary Information (ESI) available: See DOI: 10.1039/b000000x/

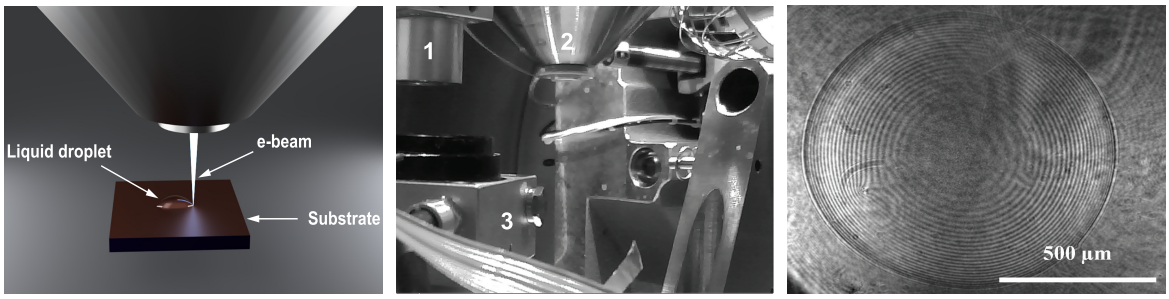

(a) (b) (c)

Fig. 1 (a) Illustration of liquid phase focused electron beam induced process in which the electron-beam drives reactions near a liquid-solid interface (b) Optical imaging system installed in the ESEM chamber that utilizes interferometry to visualize and measure the thickness of liquid films. The labels 1, 2, and 3 indicate the optical system, electron final lens, and cooling stage respectively. (c) Interferogram of 5M H_2SO_4(aq) droplet using 660 nm wavelength light. The interference fringe pattern is used to estimate liquid film thickness vs. position.

tron beam promises to overcome many of the challenges associated with gas phase-FEBIP and offers several potential advantages.[32,41–47] These include providing access to materials with no known/elusive gas-phase precursors, higher throughput, less toxic products, increased stability, lower cost, and charge dissipation when using insulating substrates. Much of the prior work in liquid phase-focused electron beam induced process (LP-FEBIP) has been focused on using a sealed liquid cell with an electron transparent membrane to deposit nanoparticles or more complex patterns[4,23,32,42,48–53]. Sealed cells have also been used to study the oxidative etching of nanoparticles driven by the electron beam.[1,4,6,9,10] Controlled etching of silicon nitride membranes[46,48] and the accelerated corrosion of copper[54] have also been observed in sealed cells.

However, the necessity of utilizing a closed cell severely restricts the practical utility of this technique. For example, one cannot work on complex samples such as integrated circuits. Restricted substrate choices and membrane damage[8,32,50] also limit one's ability to study the process under the wide range of beam conditions critical to understanding LP-FEBIP. Recently, more practical techniques have been developed to allow direct processing on bulk substrates by using thin liquid layers. The liquid can be introduced by in-situ hydration,[41,44] injection from a capillary,[11,44,55] or by nanoelectrospray.[47,56] Depending on the technique and reactants the processes can be carried out in high vacuum or, in the case of this work, in a variable-pressure environmental scanning electron microscope (ESEM) as shown in Fig. 1.

This approach enabled the deterministic electron-beam induced etching of various copper films on silicon substrates utilizing aqueous sulfuric acid as the etchant.[11]. Sulfuric acid has considerable benefits as an e-beam induced copper etchant including (1) no spontaneous etching at lower concentrations and temperatures, (2) low vapor pressure,[57] (3) previous use in vacuum systems (Auger spectroscopy),[58] (3) concentration control in a surrounding of water vapor,[59] (4) removal of native copper oxide, and (5) production of soluble by-products for Cu etching process.

The challenges associated with etching copper for circuit edit using FIB, combined with the successful use of liquid reactants in LP-FEBIP, made it desirable to investigate the process of LP-FEBIE of copper more in depth. Thus, the goals of this work are to 1) provide a comprehensive investigation into the copper etching process using LP-FEBIE involving liquid thickness and beam current; 2) develop a predictive model for LP-FEBIE of copper; and 3) enhance understanding of the LP-FEBIE radiation chemistry. After developing *in-situ* interferometry to measure liquid thickness, we found that etch rate increases with both thickness and beam current. However, the dependence is sublinear because of the complicated interplay of electron scattering with radical reactions and transport. We also found that a hybrid Monte Carlo-continuum model can capture this complexity and successfully predict the copper etch rate.

2 Results and Discussion

2.1 Focused Electron Beam Induced Etching with Controlled Liquid Thickness

The thickness of the liquid film is critical for understanding and controlling the LP-FEBIE process. Specifically, pattern accuracy and uniformity, repeatability, mass transport, and electron scattering are all affected directly by liquid thickness.[11,41,44,45] Moreover, the liquid thickness can be manipulated by changing sample temperature and gas pressure in the chamber to alter the equilibrium volume and control wetting of the substrate.

Previous efforts to determine liquid thickness *in-situ* include pre-deposition of vertical pillars on a substrate to form a "nano ruler."[47] Although effective, this technique limits the range of thicknesses than can be measured and requires modification of the substrate. In addition, the presence of the pillars can alter wetting of the liquid and reshape the meniscus. We also considered using energy dispersive x-ray spectroscopy (EDX) to determine liquid thickness, but this technique requires repeatedly solving the inverse x-ray generation problem from a layered sample with the added challenge of working in a water-vapor ambient.

The limitations of these techniques led us to design and implement an *in-situ*, optical imaging system that allows direct measurement of the liquid thickness and visualization of the liquid thin film topology. The system enables liquid-phase FEBIE with controlled liquid thicknesses in an ESEM as shown in figures 1b and 1c. In contrast to previous work on integrated correlative

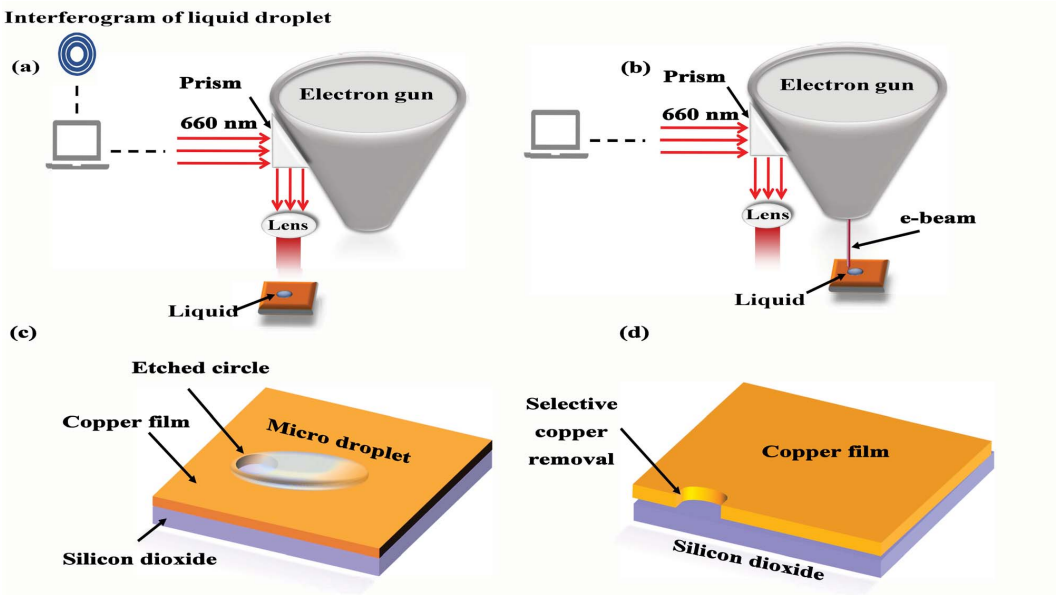

Fig. 2 Schematic of copper etching process using liquid phase FEBIE with controlled liquid thickness. (a) Measuring liquid thickness interferometrically and imaging droplet topography. (b) Exposing the sample to the electron beam to perform etching. (c) Enlarged view of the sample with the microdroplet of reactant. (d) A cross sectional view of an etched feature after exposure.

light and electron microscopy (iCLEM) for imaging and spectroscopy,[60,61] our system employees interferometry to determine the thickness of a structure, in this case a microdroplet, on a substrate.

An example interferogram of an aqueous sulfuric acid droplet is shown in Fig. 1c. The concentration of sulfuric acid,[59] and thus its refractive index,[62] can be estimated from the temperature of the sample and the water vapor pressure in the chamber. As expected, the interference fringes, corresponding to changes in thickness of 240 nm, are closely spaced at the periphery of the droplet where the liquid thickness changes rapidly. Changes in droplet spreading and topology with temperature and pressure can be easily visualized, and fiducial marks allow registration between the optical and electron imaging systems.

During etching experiments, we first moved the sample under the optical system to estimate liquid thickness *in-situ* before exposing it to the electron beam (Fig. 2a). Second, we moved the sample under the e-beam, (Fig. 2b), to perform copper etching at the desired liquid thickness. Finally, we moved the sample back to the optical system to confirm that the thickness had not changed, other than in the etched feature, during etching. The etched volume was measured using the SEM *ex-situ* in high vacuum mode and the results were compared to our hybrid Monte Carlo/continuum model discussed below.

An example etching experiment with controlled liquid thickness is shown in Fig. 3. A marked difference can be seen in the feature size between the 240 and 480 nm thick regions of the liquid layer in both tilted, (Fig. 3a), and cross-sectional, (Fig. 3c), electron micrographs. A detailed discussion of the liquid thickness and beam current dependence, as well as comparison to model predictions, is presented below. However, it is clear that control of liquid thickness with the correlative optical system is essential for controlling the etch process.

For many etching tasks one wishes to achieve a given geometry by scanning the beam over a defined area. *In-situ* determination of liquid thickness allows us to determine the process window for such a standard etch process. We exposed $2\,\mu$m diameter circular areas using a spiral scan strategy from the center to the edge of the circle with a step size 0.8 nm and curve step size of 16 nm. For each pattern, the areal dose was adjusted by changing the dwell time per point. A set of etches were conducted with 30 keV and 0.216 nA beam current at constant liquid thicknesses of 240 nm and 480 nm. The dose was varied from $1.5\,\mathrm{C/cm^2}$ to $4.5\,\mathrm{C/cm^2}$ with an increment of $0.5\,\mathrm{C/cm^2}$. As shown in Fig. 4a, doses of $2.0\,\mathrm{C/cm^2}$ and lower resulted in incomplete Cu film removal. Doses of $2.5\,\mathrm{C/cm^2}$ and greater were adequate to sufficiently remove the $1\,\mu$m electrodeposited Cu film revealing the underlying barrier layer. Further increasing the dose expands the etched region laterally as shown in Fig. 4b. A dose of $\approx 2.3\,\mathrm{C/cm^2}$ yielded the best match between the designed pattern and the etched feature for both liquid thickness. Thus, we find that feature sizes can be well controlled by electron dose over a range of liquid thickness when the liquid layer is thin compared to the copper.

2.2 Hybrid Model for Liquid-phase FEBIE

The underlying chemical and physical processes involved in LP-FEBIE are numerous and complex; as a result, the relationship of feature size and etch rate to other variables has also been challenging to predict. These processes include electron interactions with water vapor in ESEM chamber, with the liquid reactant, and with the solid substrate, all of which depend on the geometry and primary electron energy. In addition, radiolysis products in the liquid diffuse and react with other species as well as the material to be etched. These reactions depend on the volumetric dose rate which is governed by the electron-beam current, beam energy,

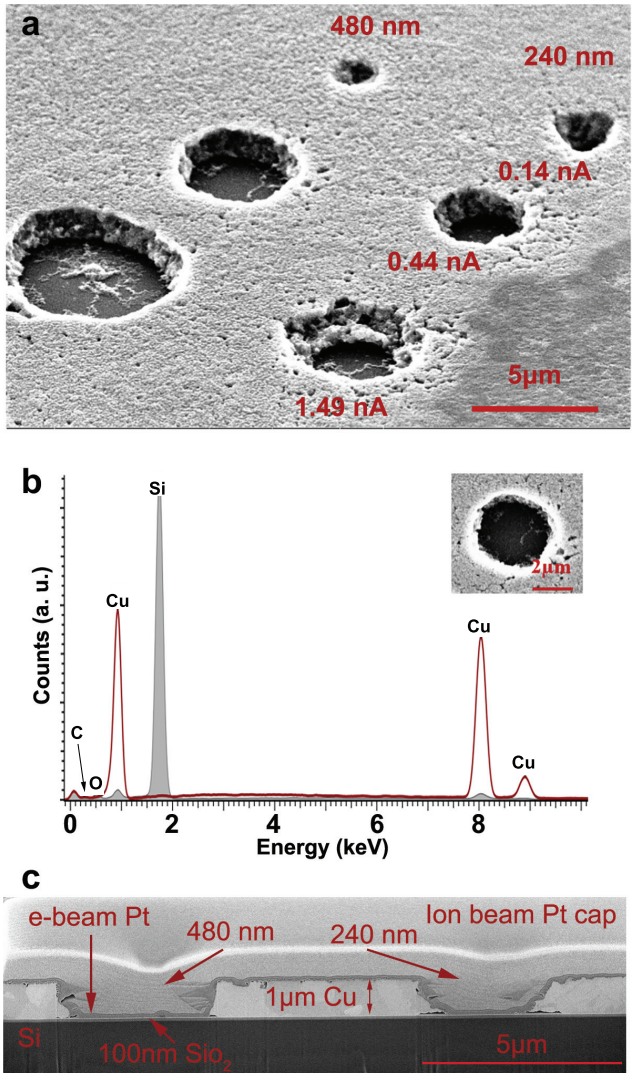

Fig. 3 (a) Tilted SEM micrograph, 50°, of features etched into a 1 μm thick electrodeposited Cu film using 5M H_2SO_4 at 30 keV for 180 s with 0.14, 0.44, and 1.49 nA (labeled) beam currents. The circles at the right were etched at 240 nm liquid thickness while the circles at left were etched at 480 nm. (b) EDX spectra of etched feature and 1 μm Cu on Si demonstrating complete removal of Cu in the etched area (gray signal) compared to the unetched area (red signal). (c) Cross sections of the etched circles in (a) etched with 0.442 nA beam current at 240 nm and 480 nm liquid thickness, labeled, clearly show the complete removal of Cu without damaging the underlying layer.

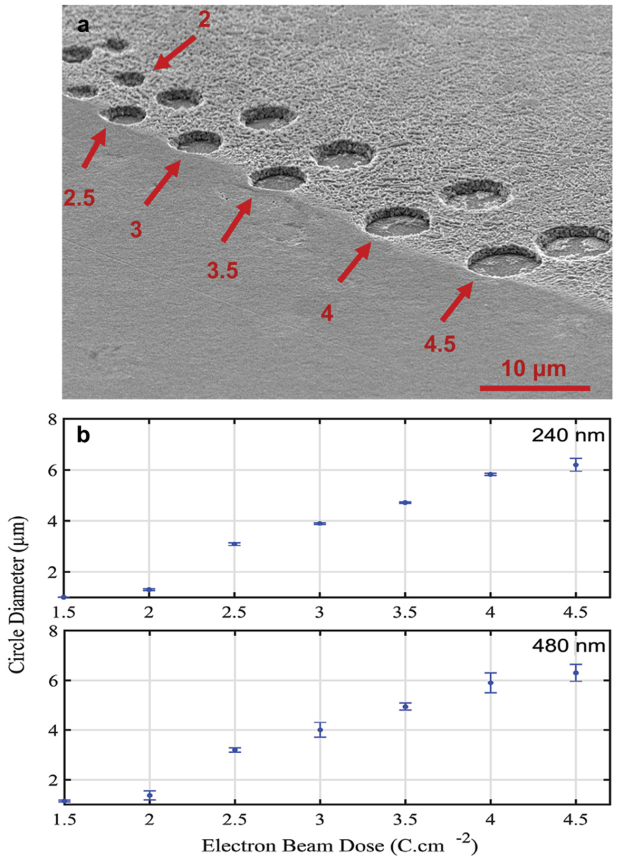

Fig. 4 (a) Ex-situ micrograph of circles etched into a 1 μm thick electroplated Cu film with increasing doses in C/cm^2 and two liquid thicknesses. 480 nm (top row) and 240 nm (bottom row). (b) Measured diameter of etched circles vs. electron beam dose from (a) using 240 and 480 nm thick liquid.

and scattering. The significant dependence on liquid thickness further complicates our understanding of this process.

Clearly, physical and chemical models of the process would both enhance our understanding and accelerate selection of etch conditions for various applications. Now that experiments can be conducted with controlled liquid thicknesses, as described above, there is strong motivation to develop a predictive model for e-beam induced etching in liquid. Toward this end, we combined Monte Carlo simulation of electron scattering with continuum (finite element) simulation of the solution chemistry and etch process. Fig. 5 shows a schematic of the simulation procedure.

The Monte Carlo model provides the energy deposited by electrons as a function of position in the liquid as they scatter and lose energy as shown in Fig. 5b. JMONSEL,[63] a Monte Carlo method based computer program developed by NIST, was used to simulate electron interaction with the gas in the chamber and the liquid and to track energy loss. The Monte Carlo output becomes the input to a finite element model that calculates radical generation and the concentration vs. position of all reactants accounting for diffusion and reactions in solution. This model also monitors Cu etching and the moving boundary between the liquid and the solid as shown in Fig. 5c. The finite element portion of the model was realized in COMSOL Multiphysics. MATLAB interface code was used to convert the Monte Carlo output (energy vs. position in 3D Cartesian coordinates) to a 2D radially symmetric input to the finite element code.

Monte Carlo Modeling of Electron Scattering and Energy Deposition

JMONSEL tracks primary electrons (PEs) and secondary electrons (SEs) and the energy deposited by them. Regions are defined by shapes and material. Different regions can have different materials and material properties. These include, but are not limited to, scattering mechanisms, energy loss mechanisms and the minimum energy to track SEs. In our simulation, the chamber volume contains two regions: a water vapor layer and a liquid

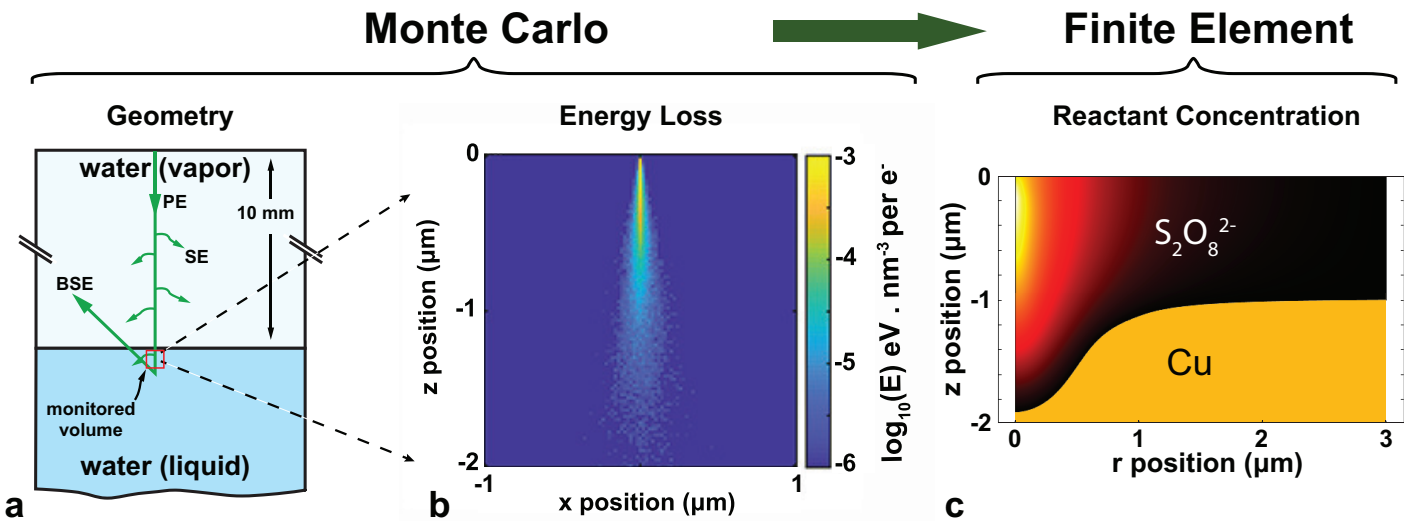

Fig. 5 Schematic of the simulation steps of LP-FEBIE of copper showing the role of each simulation code. (a) Illustration of the electron Monte Carlo simulation in JMONSEL showing primary (PE), secondary (SE), and backscattered (BSE) electrons. (b) Example plot of average energy deposited vs. position in the liquid reactant. (c) An example plot of an etchant species, $S_2O_8^{2-}$, concentration vs. position during the Cu etch. The deformed boundary of the liquid-copper interface from etching is also shown.

water layer. The water vapor was treated as a layer of low-density water with a thickness of 10 mm corresponding to the experimental working distance. The long working distance was chosen to be consistent with other experiments in which EDX analysis was used for solution characterization. JMONSEL converts composition, pressure, and temperature into a material with the given composition and density. Electron elastic and inelastic scattering in the water vapor was simulated using the Egerton atomic model for the gas scattering cross section.[64] The water vapor thickness was 10 mm with a pressure of 4.9 Torr and temperature of 10°C. Unlike the Rutherford and Mott models that calculate the elastic cross section only, the Egerton model accounts for inelastic scattering using a ratio of the inelastic to elastic scattering cross-sections. Egerton proposed a ratio of $\sigma_i/\sigma_e = C/Z$ where Z is the atomic number and the constant, C, is a weak function of beam energy and Z. Calculated values for C include 17 for 50 keV electrons and 18 for 100 keV electrons.[64] Experiments support a value of 20 for 80 keV electrons.[64]

Using $C = 17$ and the elastic scattering cross sections for H and O from the NIST SRD 64 database[65] for 30 keV we find that $(\sigma_i/\sigma_e)_{H_2O} = 3.2$. Treating the water molecule as a single scatter with Z=10 would yield $(\sigma_i/\sigma_e)_{H_2O} = 1.7$. Mansour *et al.*.[66] measured a scattering ratio of 2 for water vapor. Additionally we computed the probability of electrons traversing the water without scattering using a Poisson distribution[67] and experimental data for the average number of collisions measured by Wight *et al.*.[68] The probability is a function of scattering cross section, number of atoms per unit volume and the gas path length. The number of un-scattered electrons compared favorably with simulations using a scattering ratio of 2. Thus, we conducted all simulations using a scattering ratio of 2 which is consistent with both others' experimental data and the range of values expected from the Egerton ratio.

In the liquid, the screened Rutherford cross section was used to model elastic scattering while the Joy-Luo-Nieminen[69,70] model was used for the inelastic scattering. For the latter model, we used a work function of 4.8 eV based on a mid-gap placement of the Fermi level given the bandgap and electron affinity of liquid water.[71–73] This is consistent to within ± 0.2 eV of that found for aqueous solutions as well.[74,75] The stopping power in liquid water as a function of electron energy was extracted from the combined data sets presented by Francis *et al.*[76–79] by fitting the Joy-Luo-Nieminen model with two free parameters: the effective energy required to generate a secondary electron and the low-energy cutoff for the transition from the Joy and Luo form to the Nieminen form.

The extracted parameters were validated by simulating the secondary electron yield from liquid water and comparing with the experimental data of Thiel and Suszcynsky.[80,81] Good agreement was found at primary electron energies $\geq$ 2 keV. (See supporting information, Fig. S1). Below 2 keV experimental SE yields from water diverge based on the sample details,[80,82,83] and so the poorer agreement in this region is less concerning. Moreover, the limited range of these lower energy secondaries[84] lessens their impact on the simulation results as discussed in the supplementary information. With the required parameters in place and the confidence gained by comparison with others' experimental results, the Monte Carlo simulation was used to extract deposited energy vs. position in the liquid under the experimental conditions employed here.

To reduce computation time the Monte Carlo simulations were conducted once with an infinite liquid. As the continuum simulation progressed, the energy loss in the finite liquid layer was extracted from the infinite liquid results based on the liquid geometry at the relevant time point. This approximation captures the spatial and temporal evolution of radical generation without requiring repeated Monte Carlo simulations. However, it does neglect backscattering of primary electrons and emission of sec-

ondary electrons from the copper, though not backscattering and secondary electron generation in the liquid itself. Neglecting backscattered electrons is strongly justified because backscattered electrons from the substrate, at the energy of interest, typically increase absorbed energy density only a fraction of a percent in the irradiated layer.[85]

In TEM studies at high primary electron energies ($\sim$ 300keV) the energy loss in the liquid is nearly uniform with depth while secondary emission from a high-atomic-number metal wall can be substantial.[86] This leads to higher relative dose rates near interfaces. However, in the current study we can neglect this phenomenon because of the greatly increased energy loss of 30 keV primary electrons near the top of the liquid film and the lower SE generation at the copper-water interface.

Continuum Modeling of Etch Process

After establishing the energy loss versus position, we used finite element analysis to model radical generation, subsequent reactions, reactant transport, and etching at the copper-liquid interface. Details of the finite-element model formulation are provided in the supplementary information. Rate constants used in the model are given for each relevant reaction, and diffusion coefficients for each species are noted as well. As noted above, experimental results for electron beam induced etching of Cu in H_2SO_4 suggest a radiation-based Cu etching mechanism.[11]

During radiolysis, radical species are formed in the irradiated volume due to energy transfer from the electrons to the reactants. Our energy deposition model assumes that discrete radiolysis events can be approximated by a continuous radical generation rate. This rate is given by the product of the radical yield, experimentally determined by others in bulk solutions, and the average energy deposition rate in each Monte Carlo voxel. This assumption enables the continuum modelling of etching and offers much faster execution than a full kinetic Monte Carlo model. However, this assumption would need to be revisited if the spatial and temporal statistics of the radiolysis process became significant. This would be the case, for example, if one wished to study the surface roughness of features approaching the voxel size or features etched using only a few primary electrons.

Irradiation of aqueous sulfuric acid[87–90] produces sulfate radicals by the following mechanisms:

$$HSO_4^- \xrightarrow{\text{PE}} H + SO_4^- \quad (1)$$

$$H_2O \xrightarrow{\text{PE}} H + OH \quad (2)$$

$$OH + HSO_4^- \longrightarrow H_2O + SO_4^- \quad (3)$$

$$OH + H_2SO_4 \longrightarrow SO_4^- + H_3O^+ \quad (4)$$

The first of these processes, direct radiolysis of HSO_4^- (reaction 1), is fast compared to the timescale of the other processes considered here.[87,88,90] Jiang reported the yield of the sulfate radical for reaction 1 to be $f_s G_f$ where f_s is the electron fraction of sulfuric acid and $G_f = 2.8$ SO_4^-/100 eV. For the sulfuric acid concentration considered here this translates to a yield of 1.0 SO_4^-/100 eV. The secondary pathway through the OH radical (reactions 3,4, $k_3 = 4.7 \times 10^5$ and $k_4 = 1.4 \times 10^7$ L mol^{-1} s^{-1})) is much slower and there are at least four additional competing reactions.[87] We neglected this slower and more complex pathway in our simulations and still achieved excellent agreement with experiments as discussed below. Also following Jiang, we did not differentiate between the action of the primary electrons on H_2SO_4, HSO_4^-, and SO_4^{2-} in solution. Likewise we did not track the concentrations of the three species separately, but rather treated them all as HSO_4^-.

The sulfate radical is a strong oxidizer with a standard reduction potential from 2.5 to 3.1 V[91] and is certainly capable of oxidizing copper metal to Cu_2^+(aq). In addition to oxidizing copper, the sulfate radical can either recombine with atomic hydrogen or combine with itself as shown below.

$$H + SO_4^- \longrightarrow HSO_4^- \quad (5)$$

$$2\,SO_4^- \longrightarrow S_2O_8^{2-} \quad (6)$$

Reaction 6 has a range of reported rate constants spanning 3.8×10^8 to 8.1×10^8 L mol^{-1} s^{-1} based on flash photolysis measurements. The value listed below represents the median value rounded to one significant figure.[91] Atomic hydrogen formed in reaction 1 can be removed from subsequent reactions through the formation of H_2(g).[92]

$$H + H \longrightarrow H_2(g) \quad (7)$$

The peroxydisulfate ($S_2O_8^{2-}$) ion is also a strong oxidizer (standard reduction potential of 2.05 V[77]) and is commonly used to etch copper. Thus, either the radical or the resulting ion will serve as an effective etchant. At the surface the oxidizing species (SO_4^- and $S_2O_8^{2-}$) react with Cu and aqueous Cu^{2+} forms as follows:

$$2\,SO_4^- + Cu(s) \longrightarrow Cu^{2+}(aq) + 2\,SO_4^{2-} \quad (8)$$

$$S_2O_8^{2-} + Cu(s) \longrightarrow Cu^{2+}(aq) + 2\,SO_4^- \quad (9)$$

For simulation purposes these reactions are assumed to be instantaneous, and the multistep oxidation of copper was not considered. The density of electroplated copper was taken as the bulk density.

The simulations reveal several important aspects of the etching process. First, under the electron beam conditions considered here, irradiation of the solution does not locally deplete HSO_4^-. As shown in Fig. 6a, the HSO_4^- concentration is reduced by less than 0.1% compared to its initial concentration. This is at the location of highest energy transfer, but elsewhere the change is considerably smaller. This result gives us confidence that we can model the transport of other reactants as dilute species in a homogeneous aqueous sulfuric acid solution. This also confirms the assumption that we do not need to consider non-uniform sulfuric acid concentration in our Monte Carlo simulations.

Secondly, we find that the sulfate radicals rapidly combine in the irradiated region, and that peroxydisulfate ($S_2O_8^{2-}$) is the primary copper etchant. As shown in Fig. 6b the sulfate radicals are confined to the volume of highest energy transfer. Fig. 6c

shows the much greater range of of the peroxydisulfate ion. An example data set showing peroxydisulfate concentration and etch progression as a function of time is shown in supplementary Fig. S2.

The finite element simulations described above do not consider the concentration of Cu^{2+} in solution, nor do they account for reduction of copper ions or oxidation of metallic copper in the liquid. However, if the concentration becomes sufficiently high then the rate of reduction of Cu^{2+} back to Cu metal may become significant. In fact, we did observe copper re-deposition when we tried to quickly etch large arrays of densely packed features using high beam currents as shown in Fig. 7. Under normal conditions, atomic hydrogen produced by radiolysis will recombine with the sulfate radical or react with itself to produce hydrogen gas. Likewise, solvated electrons will be rapidly scavenged by $H^+ + e^-(aq) \longrightarrow H$ ($k = 2.5 \times 10^{10}$ L mol^{-1} s^{-1}).[93] However, in the presence of high concentrations of Cu^{2+}, both reducing species (H and $e^-(aq)$) may react with Cu_2^+ instead. (reactions 10 and 11.) Cu^+ may be returned to Cu_2^+ by reaction with hydrogen (reaction 12) or be further reduced to copper metal by disproportionation (reaction 13).

The relevant reactions are

$$Cu^{2+} + H \longrightarrow Cu^{1+} + H^+ \quad (10)$$

$$Cu^{2+} + e^-(aq) \longrightarrow Cu^{1+} \quad (11)$$

$$Cu^+(+H^+) + H \longrightarrow Cu^{2+} + H_2(g) \quad (12)$$

$$Cu^+ + Cu^+ \xrightarrow{\text{fast}} Cu^0(s) + Cu^{2+} \quad (13)$$

Thus, it was important to maintain sufficiently low pattern density and etch rates to prevent such deposition in the experiments described below. Moreover, future work should consider simulating reduction reactions in addition to oxidation reactions.

We also note that these simulations did not include thermal effects such as heat transfer or advection but still yield good agreement with experiment. It is likely that working with a thin liquid on a high thermal conductivity substrate is important in this regard. This is consistent with Rykaczewski et al.'s work showing there was no measurable e-beam induced evaporation of water droplets on silicon whereas there is substantial evaporation on superhydrophobic nanowires.[94] Finally, we note that these simulations are restricted to radially symmetric cases, and that simulation of more complex patterns will require full 3D analysis as well as consideration of the time-dependent beam deflection strategy.

The values of the rate constant ($k_{no.}$ in L mol^{-1} s^{-1}) of the reactions discussed above are $k_3 = 4.7 \times 10^5$,[87] $k_4 = 1.4 \times 10^7$,[87] $k_5 = 1 \times 10^{10}$,[87] $k_6 = 5 \times 10^8$,[91] $k_7 = 7.8 \times 10^9$,[93] $k_{10} = 9 \times 10^7$,[93] $k_{11} = 3.3 \times 10^{10}$,[93] $k_{12} = 1.3 \times 10^{10}$.[95] The values of diffusion coefficients (D_X) in m^2 s^{-1} are $D_{HSO_4^-} = 1.385 \times 10^{-9}$,[62] $D_{SO_4^-} \approx D_{SO_4^{2-}} = 1.065 \times 10^{-9}$,[62] $D_{S_2O_8^{2-}} = 1.1 \times 10^{-9}$,[62] and $D_H = 8 \times 10^{-9}$.[93]

2.3 Influence of liquid thickness and electron beam current on the etch rate

As discussed above, the number of oxidizing species (SO_4^- and $S_2O_8^{2-}$) produced is directly related to the energy lost in the liquid. The thicker the liquid the more energy is lost, and thus one would expect a general increase in etch rate with liquid thickness. The electron beam current also directly controls the generation rate of oxidizing radicals by altering the number of electrons impinging on the liquid per unit time. Thus, the etch rate is expected to increase with beam current. However, these relationships will be complicated by dose rate effects and subsequent reactions in the liquid. For example, when irradiating a liquid with a high-brightness, focused electron beam the local dose rate can be much higher than that observed in typical radiation chem-

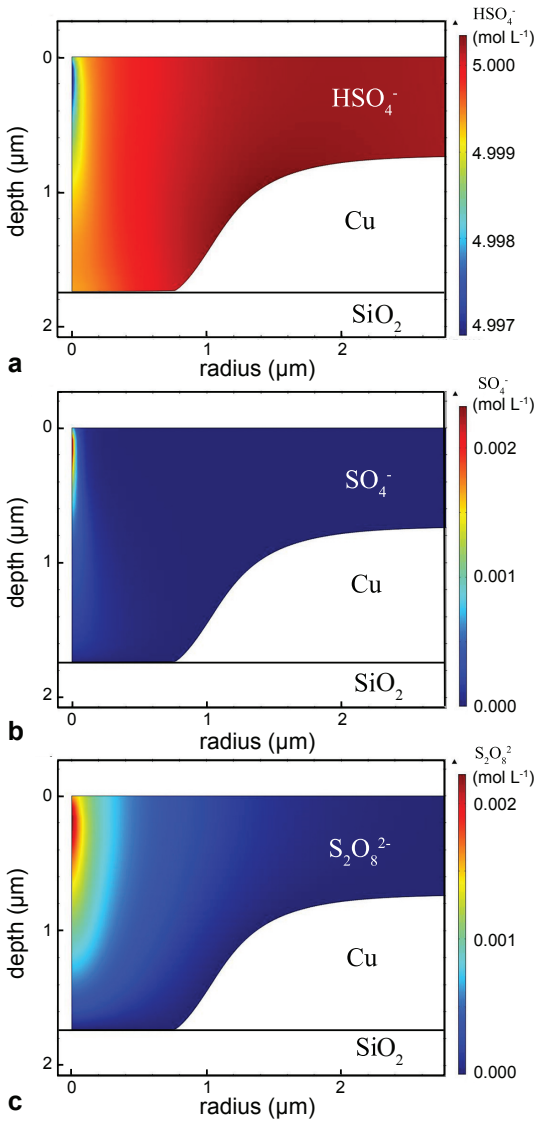

Fig. 6 Hybrid simulation showing HSO_4^- (a) and SO_4^- (b) and $S_2O_8^{2-}$ (c) concentrations when the solution is irradiated at 30 keV, 0.442nA, and 730 nm liquid thickness. The image represents a cross-section of an axially symmetric simulation. $S_2O_8^{2-}$ is the primary copper etchant. The plots were generated at a time point of a 180 second.

istry experiments with bulk samples and large area, MeV electron sources.

Given these expectations, experiments were conducted in which the volumetric etch rate ($\mu m^3\ s^{-1}$) was measured as a function of liquid thickness and beam current. The liquid thickness refers to the initial thickness at the beginning of the etch process. We assume that the liquid fills the etched feature on a time scale that is short compared to the overall etch time. All etched features were assumed to have a cylindrical shape for volumetric calculations. The results of these experiments were compared to model predictions.

The primary electron energy was fixed at 30 keV, and five beam currents (0.14, 0.44, 1.50, 4.98, and 5.95 nA) were investigated. Patterns were exposed using a spot scan at liquid thicknesses of 240 nm, 480 nm, and 730 nm for 180 seconds. At least seven etches were performed at each combination of beam current and liquid thickness and a total of more than 170 features were etched and measured. As expected, etched feature size demonstrates a strong dependence upon both liquid thickness and beam current as can be seen in Fig. 3. Fig. 8 quantifies these relationships and compares them to the hybrid Monte Carlo/continuum model discussed above. First, the simulated and experimental etch rates agree remarkably well given that all required model inputs were measured (beam current, beam energy, and liquid thickness) or obtained from studies conducted by others (scattering cross-sections, stopping powers, radical yields, secondary electron yields, diffusion coefficients, and reaction rates). There were no fitting parameters used in the simulation.

We found that the etch rate increases monotonically with beam current and saturates at higher beam currents. Our hybrid model predicts quantitatively similar behavior. The initial increase in etch rate with current reflects the increased generation rate of oxidizing radicals. This parallels the electron- or ion- limited regime in gas-phase beam-induced etching where etch rates are limited by the rate of charged particle arrival. For example, Schoenaker *et al.* note a similar effect in FEBIE of titanium using XeF_2.[96]

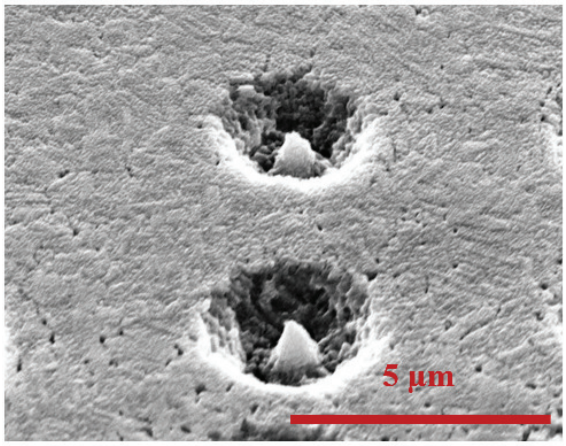

Fig. 7 Tilted view of an SEM micrograph of 120 s spot scan etched into $1\,\mu m$ electroplated Cu at 30 keV and 0.44 nA showing redeposited material.

The saturation of the etch rate at higher currents could be the result of either reactant (HSO_4^-) depletion or more complex subsequent reactions. As discussed above, our simulations show that the reduction in concentration of HSO_4^- is no more than 0.1% even in the volumes with the highest local dose rate. Rather, it is conversion of atomic H to $H_2(g)$ and the time evolution of the geometry that yields a nonlinear etch rate dependence. This contrasts with gas phase processes at higher beam currents in which the etch rate is limited by the depletion and mass transport of reactants.[12,96,97] In fact, the provision of large reactant concentrations is one of the key advantages of liquid-phase processes.

Although almost all of the experiments in Fig. 8 agree well with simulation, there appears to be a deviation between the experimental and simulated data at the higher beam currents (5 and 6 nA) and thickest liquid ($730\,\mu m$). Some possible reasons for this deviation include accelerated etching by heating, radiolysis of reaction products that is only significant at high dose rates, and/or an increase in beam spot-size that reduces dose-rate effects.

3 Conclusion

Localized etching of Cu is critical for many nanotechnology-related applications, and using an electron beam with a liquid reactant avoids many of the negative aspects of FIB etching. For the case of copper etching in aqueous sulfuric acid, the etch products are soluble and the etch chemistry is highly selective to other materials leading to clean, precise copper removal. Moreover, pressure and temperature can be used to control the concentration and thickness of the liquid while interferometric imaging allows direct measurement of liquid thickness. This combination provided dimensional control of etched features and allowed the development of a predictive model for the etch process. Excellent agreement between simulated and experimental etch rates was obtained using data from the radiation chemical and electron microscopy literature without any fitting parameters. Under the conditions considered here, etch rate increases with both liquid thickness and beam current, but in a nonlinear fashion governed by electron energy loss, dose rate, and reactions in the liquid.

Both the experiments and simulations presented here were oriented toward removal of larger volumes of copper ($\sim \mu m^3$) characteristic of upper metal layer circuit editing. Future work will focus on higher resolution processes for which both the liquid thickness and gas path length will be reduced. In addition, future development of the simulation code will allow re-simulation of the electron energy deposition at additional time steps to more accurately capture the early stages of the etch process. Complete optimization of the process will also require evaluation of primary beam energy, reactant concentration, and beam scanning and blanking strategies. However, now these effects can be explored confidently in simulation to greatly accelerate the design of experiments.

4 Experimental Methods

4.1 LP-FEBIE

The etching experiments were carried out using an environmental scanning electron microscope (ESEM, Quanta 250 FEG, Thermo

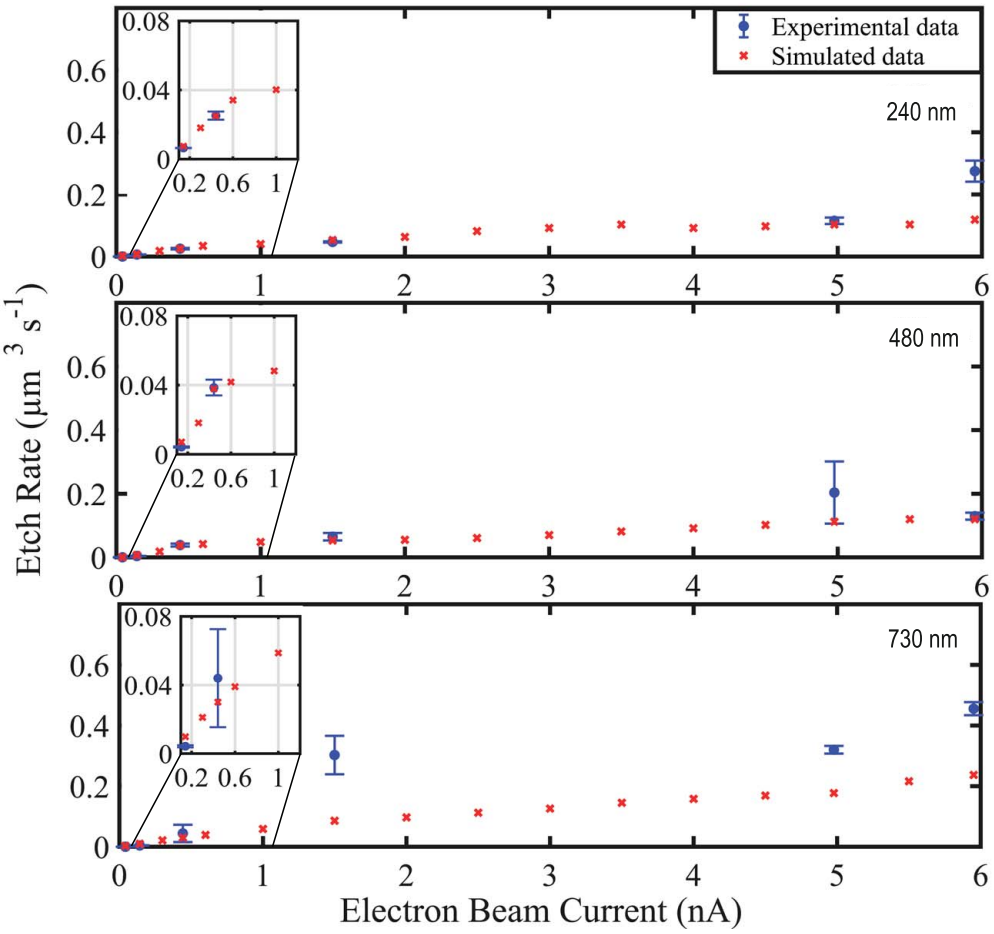

Fig. 8 Experimental and simulated data for copper etch rate as a function of beam current and liquid thickness. The experimental and simulated results agree quantitatively at all but the largest currents and liquid thicknesses. Data from over 170 etched features is included and no fitting parameters were employed to match simulated and experimental results.

Fisher Scientific, Hillsboro, OR, USA). A gaseous secondary electron detector (GSED) was used to collect secondary electron signals (SE) in the ESEM. A Peltier cooling/heating stage was used to carefully control sample temperature and hence, the condensation and evaporation of water from the sulfuric acid solution on the surface. Silicon wafers with 1 μm thick electrodeposited copper film on 30nm Cu/Mn, 7nm Ta, 7nm TaN, 100 nm SiO_2 were cleaved into segments less than five by five mm to fit in the Peltier stage. Each sample was rinsed thoroughly with isopropyl alcohol (IPA, Fisher Scientific) then deionized water (DI) to remove any trace of the alcohol. Next, each sample was dipped in sulfuric acid for 15-20 seconds to remove any copper oxide (CuO_x). Samples were fixed to the Peltier stage with conductive silver paste (TED PELLA, INC.) to ensure adequate thermal conductivity.

Sulfuric acid (H_2SO_4) (EMD chemicals Inc.) was used as the reactant for etching. Before pumping the ESEM to vacuum, a microdroplet of 1 M H_2SO_4(aq) was pipetted directly onto the substrate. Much of the liquid was then pulled back into the pipette, leaving a relatively shallow layer of liquid on the substrate. This better facilitated the use of both the optical system and the etch process, *in-situ*, by providing a more gradual gradient of droplet thickness. Initially, the substrate temperature was set to three degrees Celsius (3°C) and ESEM chamber pressure to 5.5 Torr to maintain the initial 1 M concentration of H_2SO_4. The concentration of H_2SO_2 was controlled *in-situ* through manipulation of chamber pressure (water vapor) and sample temperature. The condensation and evaporation of water vapor leads to a change in sulfuric acid concentration as reported by Massucci *et al.*[59]. For all experiments, the chamber pressure was reduced to 4.9 Torr, and the temperature was raised to 10°C. This led the H_2SO_4 concentration to increase to 5 M.

The effect of beam current and liquid thickness on the etch rate were studied. Beam current was investigated over currents ranging from 0.14 nA to 5.95 nA. The beam current was measured using a Keithley picoammeter and a Faraday cup. A stationary beam at single pixel (spot scan mode) was used at intervals of 180 seconds covering a range of various liquid thicknesses.

After each etching experiment, the sample was rinsed thoroughly with DI water for at least 30 seconds, then imaged in the high vacuum mode of ESEM. Energy dispersive X-ray analysis (EDX) of elemental composition was performed using an Oxford X-Max detector (Oxford instruments, Concord, MA, USA) to determine how complete the film removal process was. Some of etches were cross-sectioned using a Helios NanoLab 660 Dual-

Beam TEM system (Thermo Fisher Scientific, Hillsboro, OR, USA) to examine etch selectivity.

4.2 Optical Imaging System

Before implementation, the optical properties of the imaging system were analyzed using Optics Studio (Zemax LLC, Kirkland, WA, USA). The system used in these experiments is a 4X magnification optical system with a 2mm field of view and 20 mm working distance. An aspheric lens (Thorlabs AL 1225-B) and an achromatic doublets lens (Thorlabs AC254-100-B) were used as the objective and imaging lenses correspondingly. Using an aspheric singlet as an objective, rather than a complex microscope objective, is acceptable because the system exhibits a small field and uses nearly monochromatic illumination. Such a lens also does not employ any adhesives that might compromise its vacuum compatibility.

A precision broadband optical glass window, BK7, (Thorlabs W64 1050-B) was used as an interface between the optical system and the vacuum chamber. All the optical components had an antireflective coatings from 650 nm and 1050 nm in wavelength. A CMOS camera (Point Grey Research, Inc.) was used to image the liquid film. 100 nm of indium tin oxide (ITO) was sputter coated on a 12 mm diameter glass substrate and placed before the objective lens to prevent charging by scattered electrons. Köhler illumination was used for light delivery with a 50:50 broadband cubic beam splitter. A SuperK Extreme supercontinuum source (NKT Photonics) was used to deliver light with a wavelength of 660 nm and a bandwidth of 10 nm. The bandwidth was selected to provide clear interference fringes while reducing speckle.

The mechanical assemblies and custom components were designed in CREO Parametric (PTC). When commercially available, vacuum compatible and non-magnetic opto-mechanics and fasteners were purchased (unanodized aluminum, vented as required). Custom components were machined from aluminum. All of the mechanical parts were cleaned with a 1% Alconox detergent for 15 minutes at 50°Cin an ultrasonic cleaner. Then, the parts were rinsed thoroughly with DI water to ensure that no detergent was left. Finally, the parts were rinsed sequentially with ethanol, acetone, and DI water before placing them in vacuum. Standard anodized aluminum and stainless steel optomechanics were used outside the vacuum system.

Extraction of liquid thicknesses were carried out in MATLAB to map the interference pattern position from the optical images to the corresponding position on the electron micrograph images. To implement image mapping with respect to mutual points, we intentionally marked the sample at locations near the liquid droplet edge. These marks are easily visible and are clearly identified in both the optical and the electron images.

Conflicts of interest

There are no conflicts to declare.

Acknowledgement

This material is based upon work supported by the National Science Foundation under Grant No. CMMI-1538650 and the Ministry of Higher Education and Scientific Research in Iraq. This work was performed in part at the University of Kentucky Center for Nanoscale Science and Engineering, the University of Kentucky Electron Microscopy Center, and the University of Louisville Micro and Nano Technology Center, members of the National Nanotechnology Coordinated Infrastructure (NNCI), which is supported by the National Science Foundation (ECCS-1542164). This work used equipment supported by National Science Foundation Grant No. CMMI-1125998. The authors thank Dr. John Villarrubia of the National Institute of Standards for his assistance with the JMONSEL Monte Carlo simulation code and for very helpful discussions. The authors also thank Professor Kathleen Dunn, SUNY Polytechnic Institute, for providing the electrodeposited copper samples and the University of Kentucky College of Engineering machine shop.

References

1 Y. Jiang, G. Zhu, F. Lin, H. Zhang, C. Jin, J. Yuan, D. Yang and Z. Zhang, *Nano Letters*, 2014, **14**, 3761–3765.

2 X. Ye, M. R. Jones, L. B. Frechette, Q. Chen, A. S. Powers, P. Ercius, G. Dunn, G. M. Rotskoff, S. C. Nguyen, V. P. Adiga, A. Zettl, E. Rabani, P. L. Geissler and A. P. Alivisatos, *Science*, 2016, **354**, 874–877.

3 Y. Jiang, G. Zhu, G. Dong, F. Lin, H. Zhang, J. Yuan, Z. Zhang and C. Jin, *Micron*, 2017, **97**, 22–28.

4 J. H. Park, D. A. Steingart, S. Kodambaka and F. M. Ross, *Science Advances*, 2017, **3**, e1700234.

5 M. Sun, X. Li, Z. Tang, X. Wei and Q. Chen, *Nanoscale*, 2018, **10**, 19733–19741.

6 M. R. Hauwiller, J. C. Ondry and A. P. Alivisatos, *JoVE (Journal of Visualized Experiments)*, 2018, e57665.

7 P. Sutter, B. Zhang and E. Sutter, *Nanoscale*, 2018, **10**, 12674–12682.

8 N. M. Schneider, M. M. Norton, B. J. Mendel, J. M. Grogan, F. Ross and H. H. Bau, *The Journal of Physical Chemistry C*, 2014, **118**, 22373–22382.

9 M. R. Hauwiller, L. B. Frechette, M. R. Jones, J. C. Ondry, G. M. Rotskoff, P. Geissler and A. P. Alivisatos, *Nano Letters*, 2018, **18**, 5731–5737.

10 M. R. Hauwiller, J. C. Ondry, C. M. Chan, P. Khandekar, J. Yu and A. P. Alivisatos, *Journal of the American Chemical Society*, 2019.

11 L. Boehme, M. Bresin, A. Botman, J. Ranney and J. T. Hastings, *Nanotechnology*, 2015, **26**, 495301.

12 I. Utke, P. Hoffmann and J. Melngailis, *Journal of Vacuum Science & Technology B*, 2008, **26**, 1197–1276.

13 N. Silvis-Cividjian and C. W. Hagen, *Advances in Imaging and Electron Physics*, 2006, **143**, 1–235.

14 M. Huth, F. Porrati, C. Schwalb, M. Winhold, Sachser and G. Fantner, *Beilstein Journal of Nanotechnology*, 2012, **3**, 597–619.

15 K. Edinger, *Journal of Vacuum Science & Technology B*, 1999, **17**, 3058–3062.

16 C. M. Gonzalez, R. Timilsina, G. Li, G. Duscher, P. D. Rack,

W. Slingenbergh, W. F. van Dorp, J. T. M. De Hosson, K. L. Klein, H. M. Wu and L. A. Stern, *Journal of Vacuum Science & Technology B*, 2014, **32**, 021602.

17 C. Gonzalez, W. Slingenbergh, R. Timilsina, J.-H. Noh, M. Stanford, B. Lewis, K. Klein, T. Liang, J. Fowlkes and P. Rack, Extreme Ultraviolet (EUV) Lithography V, 2014, p. 90480M.

18 J. D. Casey Jr, M. Phaneuf, C. Chandler, M. Megorden, K. E. Noll, R. Schuman, T. J. Gannon, A. Krechmer, D. Monforte, N. Antoniou *et al.*, *Journal of Vacuum Science & Technology B*, 2002, **20**, 2682–2685.

19 P. Rack, S. Randolph, Y. Deng, J. Fowlkes, Y. Choi and D. Joy, *Applied Physics Letters*, 2003, **82**, 2326–2328.

20 Y. Drezner, Y. Greenzweig and A. Raveh, *Journal of Vacuum Science & Technology B*, 2012, **30**, 011207.

21 K. Lee, *Journal of Vacuum Science & Technology B*, 1989, **7**, 1941–1946.

22 A. Folch, J. Tejada, C. H. Peters and M. S. Wrighton, *Applied Physics Letters*, 1995, **66**, 2080–2082.

23 G. Schardein, E. Donev and J. Hastings, *Nanotechnology*, 2010, **22**, 015301.

24 N. A. Roberts, J. D. Fowlkes, G. A. Magel and P. D. Rack, *Nanoscale*, 2012, **5**, 408–415.

25 R. Kunz and T. Mayer, *Journal of Vacuum Science & Technology B*, 1988, **6**, 1557–1564.

26 M. Takai, T. Kishimoto, H. Morimoto, Y. Park, S. Lipp, C. Lehrer, L. Frey, H. Ryssel, A. Hosono and S. Kawabuchi, *Microelectronic Engineering*, 1998, **41**, 453–456.

27 O. Yavas, C. Ochiai, M. Takai, A. Hosono and S. Okuda, *Applied Physics Letters*, 2000, **76**, 3319–3321.

28 P. Hoyle, M. Ogasawara, J. Cleaver and H. Ahmed, *Applied physics letters*, 1993, **62**, 3043–3045.

29 A. Luisier, I. Utke, T. Bret, F. Cicoira, R. Hauert, S.-W. Rhee, P. Doppelt and P. Hoffmann, *Journal of The Electrochemical Society*, 2005, **152**, L1–L1.

30 A. Szkudlarek, A. R. Vaz, Y. Zhang, A. Rudkowski, C. Kapusta, R. Erni, S. Moshkalev and I. Utke, *Beilstein Journal of Nanotechnology*, 2015, **6**, 1508–1517.

31 V. Halka, M. J. Schmid, V. Avrutskiy, X. Ma and R. Schuster, *Angewandte Chemie International Edition*, 2011, **50**, 4692–4695.

32 E. Donev and J. Hastings, *Nanotechnology*, 2009, **20**, 505302.

33 S. K. Islam and M. R. Haider, *Sensors and Low Power Signal Processing*, Springer Science & Business Media, 2009.

34 J.-h. Chen, D.-r. Yang and D.-l. Que, *Frontiers of Materials Science in China*, 2008, **2**, 335.

35 T. Osaka, M. Datta and Y. Shacham-Diamand, *Electrochemical Nanotechnologies*, Springer Science & Business Media, 2009.

36 B. Li, T. D. Sullivan, T. C. Lee and D. Badami, *Microelectronics Reliability*, 2004, **44**, 365–380.

37 P. Ireland, *Thin Solid Films*, 1997, **304**, 1–12.

38 A. Grill and V. Patel, *Applied Physics Letters*, 2001, **79**, 803–805.

39 J. Gonzalez, D. Griffis, T. Miau and P. Russell, *Journal of Vacuum Science & Technology B*, 2001, **19**, 2539–2542.

40 T.-S. Choi and D. W. Hess, *ECS Journal of Solid State Science and Technology*, 2015, **4**, N3084–N3093.

41 S. Esfandiarpour, L. Boehme and J. T. Hastings, *Nanotechnology*, 2017, **28**, 125301.

42 E. U. Donev and J. T. Hastings, *Nano Letters*, 2009, **9**, 2715–2718.

43 F. M. Ross, *Liquid Cell Electron Microscopy*, Cambridge University Press, 2016.

44 M. Bresin, A. Botman, S. J. Randolph, M. Straw and J. T. Hastings, *Microscopy and Microanalysis*, 2014, **20**, 376–384.

45 M. Bresin, A. Chamberlain, E. U. Donev, C. B. Samantaray, G. S. Schardien and J. T. Hastings, *Angewandte Chemie*, 2013, **125**, 8162–8165.

46 E. U. Donev, M. Bresin and J. T. Hastings, in *Nanoscale Deposition and Etching of Materials Using Focused Electron Beams and Liquid Reactants*, ed. F. M. Ross, Cambridge University Press, 2016, p. 291âĂŞ315.

47 J. S. Fisher, P. A. Kottke, S. Kim and A. G. Fedorov, *Nano Letters*, 2015, **15**, 8385–8391.

48 E. Donev, C. Samantaray, M. Bresin and J. T. Hastings, Proceedings of the 39th international conference on micro and nano engineering (MNE), 2013, pp. 16–19.

49 M. Bresin, N. Nehru and J. T. Hastings, Advanced Fabrication Technologies for Micro/Nano Optics and Photonics VI, 2013, p. 861306.

50 L. E. Ocola, A. Joshi-Imre, C. Kessel, B. Chen, J. Park, D. Gosztola and R. Divan, *Journal of Vacuum Science & Technology B*, 2012, **30**, 06FF08.

51 M. den Heijer, I. Shao, A. Radisic, M. C. Reuter and F. M. Ross, *APL Materials*, 2014, **2**, 022101.

52 R. R. Unocic, A. R. Lupini, A. Y. Borisevich, D. A. Cullen, S. V. Kalinin and S. Jesse, *Nanoscale*, 2016, **8**, 15581–15588.

53 L. Wang, J. Wen, H. Sheng and D. J. Miller, *Nanoscale*, 2016, **8**, 17250–17255.

54 S. Wee Chee, S. H. Pratt, K. Hattar, D. Duquette, F. M. Ross and R. Hull, *Chemical Communications*, 2015, **51**, 168–171.

55 S. J. Randolph, A. Botman and M. Toth, *RSC Advances*, 2013, **3**, 20016–20023.

56 J. Fisher, P. Kottke and A. Fedorov, *Materials Today Physics*, 2018, **5**, 87–92.

57 A. Jaecker-Voirol, J. Ponche and P. Mirabel, *Journal of Geophysical Research: Atmospheres*, 1990, **95**, 11857–11863.

58 D. H. Fairbrother, H. Johnston and G. Somorjai, *The Journal of Physical Chemistry*, 1996, **100**, 13696–13700.

59 S. L. C. Mario Massucci and P. Brimblecombe, *Equilibrium Vapor Pressure of H2O Above Aqueous H2SO4 at Low Tempeaeture*, ACS Publications, 1996, vol. 41.

60 P. De Boer, J. P. Hoogenboom and B. N. Giepmans, *Nature Methods*, 2015, **12**, 503.

61 F. J. Timmermans and C. Otto, *Review of Scientific Instruments*, 2015, **86**, 011501.

62 *CRC Handbook of Chemistry and Physics (OnLine)*, 2018.

63 J. S. Villarrubia, A. Vladár, B. Ming, R. J. Kline, D. F. Sunday,

J. Chawla and S. List, *Ultramicroscopy*, 2015, **154**, 15–28.
64 R. F. Egerton, *Electron Energy-Loss Spectroscopy in the Electron Microscope*, Springer Science & Business Media, 2011.
65 A. Jablonski, F. Salvat and C. Powell, *NIST Standard Reference Database*, 2010, **64**, year.
66 O. Mansour, K. Aidaoui, L. Khouchaf and C. Mathieu, *Vacuum*, 2009, **84**, 458–463.
67 G. D. Danilatos, *Advances in Electronics and Electron Physics*, Elsevier, 1988, vol. 71, pp. 109–250.
68 S. A. Wight and A. R. Konicek, *Micron*, 2012, **43**, 985–991.
69 D. Joy and S. Luo, *Scanning*, 1989, **11**, 176–180.
70 R. Nieminen, *Scanning Microscopy*, 1988, **2**, 1917–1926.
71 A. Bernas, C. Ferradini and J.-P. Jay-Gerin, *Chemical Physics*, 1997, **222**, 151–160.
72 A. P. Gaiduk, T. A. Pham, M. Govoni, F. Paesani and G. Galli, *Nature Communications*, 2018, **9**, 247.
73 F. Ambrosio, G. Miceli and A. Pasquarello, *The Journal of Physical Chemistry B*, 2016, **120**, 7456–7470.
74 G. Olivieri, A. Goel, A. Kleibert, D. Cvetko and M. A. Brown, *Physical Chemistry Chemical Physics*, 2016, **18**, 29506–29515.
75 H. Tissot, J.-J. Gallet, F. Bournel, G. Olivieri, M. G. Silly, F. Sirotti, A. Boucly and F. Rochet, *Topics in Catalysis*, 2016, **59**, 605–620.
76 Z. Francis, S. Incerti, M. Karamitros, H. Tran and C. Villagrasa, *Nuclear Instruments and Methods in Physics Research Section B: Beam Interactions with Materials and Atoms*, 2011, **269**, 2307–2311.
77 Y. Tabata, Y. Ito and S. Tagawa, *CRC Handbook of Radiation Chemistry*, CRC Press, 1991.
78 A. Brodsky, *Physical Science and Engineering Data, Handbook of Radiation Measurement and Protection*, 1978.
79 H. Paul and M. Berger, *IAEA Report IAEATECDOC-799*, 1995, 415.
80 B. Thiel, D. Stokes and D. Phifer, *Microscopy and Microanalysis*, 1999, **5**, 282–283.
81 D. M. Suszcynsky, J. E. Borovsky and C. K. Goertz, *Journal of Geophysical Research: Planets*, 1992, **97**, 2611–2619.
82 V. Baglin, J. Bojko, C. Scheuerlein, O. Gröbner, M. Taborelli, B. Henrist and N. Hilleret, *The Secondary Electron Yield of Technical Materials and Its Variation With Surface Treatments*, 2000.
83 D. Joy and C. Joy, *Journal of Microscopy*, 2006, **221**, 84–88.
84 Nguyen-Truong, *Journal of Physics: Condensed Matter*, 2018, **30**, 155101.
85 M. A. McCord and M. J. Rooks, *SPIE Handbook of Microlithography, Micromachining and Microfabrication*, The Society for Photo-optical Instrumentation Engineers, United States of America, 1997, ch. 2.
86 T. Gupta, N. M. Schneider, J. Hun Park, D. Steingart and F. M. Ross, *Nanoscale*, 2018, **10**, 7702–7710.
87 P.-Y. Jiang, Y. Katsumura, R. Nagaishi, M. Domae, Ishikawa and Y. Yoshida, *Journal of the Chemical Society, Faraday Transactions*, 1992, **88**, 1653–1658.
88 B. Lesigne, C. Ferradini and J. Pauchaeult, *The Journal of Physical Chemistry*, 1972, **76**, 3676–3676.
89 P. Polevoi, A. Khachaturov-Tavrizian and I. Ivanov, *International Journal of Radiation Applications and Instrumentation. Part C. Radiation Physics and Chemistry*, 1990, **36**, 99–103.
90 B. Lesigne, C. Ferradini and J. Pucheault, *The Journal of Physical Chemistry*, 1973, **77**, 2156–2158.
91 P. Neta, R. E. Huie and A. B. Ross, *Journal of Physical and Chemical Reference Data*, 1988, **17**, 1027–1284.
92 J. M. Grogan, N. M. Schneider, F. M. Ross and H. H. Bau, *Nano Letters*, 2014, **14**, 359–364.
93 G. V. Buxton, C. L. Greenstock, W. P. Helman and A. B. Ross, *Journal of Physical and Chemical Reference Data*, 1988, **17**, 513–886.
94 K. Rykaczewski, J. Scott and A. Fedorov, *Applied Physics Letters*, 2011, **98**, 093106.
95 G. A. Johnson and N. B. Nazhat, *Journal of the Chemical Society, Faraday Transactions 1: Physical Chemistry in Condensed Phases*, 1984, **80**, 3455–3462.
96 F. Schoenaker, R. Córdoba, R. Fernández-Pacheco, C. Magen, O. Stephan and J. De Teresa, *Nanotechnology*, 2011, **22**, 265304.
97 S. Randolph, J. Fowlkes and P. Rack, *Critical Reviews in Solid State and Materials Sciences*, 2006, **31**, 55–89.

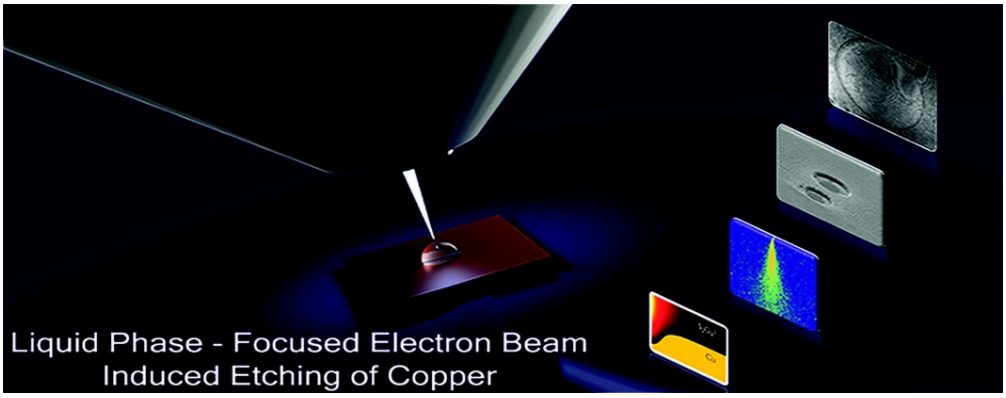

90x34mm (300 x 300 DPI)